# Charge density influence on cold fusion barriers

R. A. Gherghescu* and W. Greiner
*Institut für Theoretische Physik der J. W. Goethe Universität, Frankfurt am Main, D-60054, Germany*
(Received 15 May 2003; published 20 October 2003)

Cold fusion barriers are studied with respect to the change of the charge density within the overlapping region. Charge evolution from separated target and projectile up to the compound nucleus is taken into account by means of a deduced transition formula which depends on geometric parameter variation defining the shape. Macroscopic, shell correction and total deformation energy for fusionlike configurations are calculated for different charge density paths. Minimization along this coordinate produces variations of about 4 MeV for light nuclei and up to 8 MeV for superheavy synthesis, for the deformation energy in the last part of the process.

DOI: 10.1103/PhysRevC.68.044314 PACS number(s): 23.70.+j, 21.60.Cs, 25.85.Ca

## I. INTRODUCTION

Fusion cross sections are sensitive to deformation changes, especially for energies near the Coulomb barrier. The way geometric parameters influence the total deformation energy during the fusion process has been largely studied [1,2]. How much charge variation is responsible for the energy change and what is the mechanism through which its influence is exercised, is the main issue this work addresses.

For intermediate energy heavy-ion collisions, the isotopic composition of the emitted intermediate mass fragments, at certain energies, depends on the isospin equilibration of the composite system and on the $N/Z$ of the target and projectile as well as on the $N/Z$ of the compound nucleus [3]. Changes of the charge density in the superposed target and projectile configuration are equivalent to $Z$ (target and projectile) changes within isobaric systems. Isobaric systems have been treated for intermediate nuclei reactions, where the fusion probability for $^{82}$Se+$^{138}$Ba reaction was found very close to that of $^{40}$Ar+$^{180}$Hf, but different from $^{124}$Sn+$^{96}$Zr, for energies below the Bass barrier [4]. It is suggested that single-particle levels for the two-center system maintain a gap up to a short distance between centers, then the situation changes and friction is considered to be the cause. We will try to present charge density as a parameter responsible for structure variations near the end of the fusion process. In another approach the hypothesis of unchanged charge density is preferred for another dinuclear process, nuclear fission [5]. The evaporated neutron number is increased to preserve this constraint. Charge symmetry and asymmetry are demonstrated to differentiate between isobaric systems in Ref. [6]. At low energies, it is shown that the dependence on charge asymmetry could decide between fusion and deep-inelastic processes. Stiffness analysis concludes that a proton skin is developed in the overlapping region. Differences between coupled channels and orientation average calculation of the cross section increase with the charge product of the projectile and target, for the same synthesized nucleus in subbarrier fusion reactions [7]. This observation is related to the present work. Our calculations emphasize the role of the overlapping part in the fusion process as it is influenced by the change in the charge density of the projectile. The phenomenon induces the same effect as minimizing $Z_1Z_2$ for isobaric systems in a partially superposed configuration.

It is the influence of the charge density changes on the structure connected to the shape evolution that is treated in this work. We will show that, in the last part of the fusion process, the system acts like a different isobaric reaction. The situation is not decided for interacting nuclei fusing to form a compound nucleus, even if the system overcomes the entrance channel into the fusion barrier. This work studies a new degree of freedom for fusion reactions, the charge density of the projectile (and consequently the target) within the overlapping configuration. It is demonstrated that changes in the magnitude of the volume and in shape of the nonoverlapped part induce charge density modifications, which influence the macroscopic and shell correction energies, and accordingly the whole shape of the fusion barrier. In Sec. II the charge density variation is deduced in connection with geometric parameter changes. Section III briefly presents a very appropriate deformed two-center shell model, in order to describe the transition from two separated level schemes (target and projectile) to the compound nucleus one, within the overlapping region. A short Sec. IV reminds the main features of the macroscopic energy calculation and the suitable expression for two interacting overlapped systems. The results of fusion barrier calculation as functions of configuration parameters which influence the charge density are discussed in Sec. V, followed by Conclusions.

## II. CHARGE DENSITY VARIATION

The usual procedure to deal with different orientations of the target nucleus is to average the fusion cross section over all possible angles [1]. However, it is stressed, for example, in Ref. [8], that the barrier height for subbarrier fusion reactions increases with the collision angle for prolate deformed nuclei. Here, the value of the angle between the symmetry axis (axes) and collision axis $\theta=0°$ corresponds to tip to tip collision and produces the lowest Coulomb barrier height (the studied reaction was $^{76}$Ge+$^{150}$Nd). The effective poten-

*Horia Hulubei, National Institute for Nuclear Physics and Engineering, P. O. Box MG-6, Ro-76900 Bucharest, Romania, Email address: rgherg@ifin.nipne.ro

 

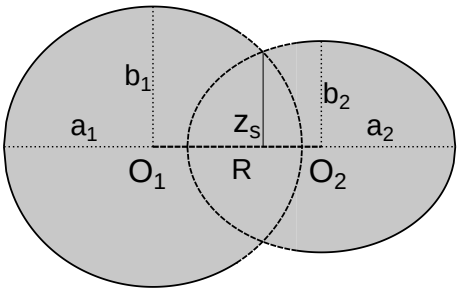


FIG. 1. Typical fusionlike shape of ellipsoidally deformed target and projectile in the overlapping region.

tial is also shown to increase for a change in angular orientation of the ellipsoidally deformed target, when the collision angle increase from 0° to 90° in $^{238}$U+16O reaction [9]. It is also emphasized that, as far as geometrical effects are concerned, when the deformed nucleus symmetry axis is rotated as to be perpendicular to the collision axis, the Coulomb barrier height increases [10]. These considerations lead us to consider only the tip to tip configuration as being energetically the most favored one. Any deviation ($\theta>0°$) produces an increase in the potential barrier. One has to mention, however, that this is true only for prolate type shapes. For $\beta<0°$ deformations (oblate shapes), the barrier becomes higher when the symmetry axis coincides with the collision one [11]. Therefore a typical nuclear configuration for fusion phenomena is described by two intersected ellipsoids with $(a_1,b_1)$ and $(a_2,b_2)$ semiaxes, separated by a plane $z=z_s$ as in Fig. 1. The two volumes are defined by the shape parameters. We will refer further on only to the left side of the shape corresponding to the heavy fragment $(A_1,Z_1)$, the demonstration for the light fragment being similar. The left side volume $(z<z_s)$ of this intermediary shape is

$$V_1=\pi\left(\frac{2}{3}a_1-\frac{z_s}{3a_1^2}+z_s\right)b_1^2. \tag{1}$$

The whole ellipsoid volume for the $(a_1,b_1)$ shape parameters is

$$V_{10}=\tfrac{4}{3}\pi a_1 b_1^2=\tfrac{4}{3}\pi R_{1x}^3=\tfrac{4}{3}\pi r_0^3 A_{1x}, \tag{2}$$

where $R_{1x}$ is the radius of the sphere having the same volume and $A_{1x}$ is the corresponding mass number. We consider the ellipsoidal shape $(a_1,b_1,z_s)$ as having the atomic properties as it were a whole nucleus $(A_{1x},Z_{1x})$; that means the charge density of the shape is determined by its geometric correspondence to $(A_{1x},Z_{1x})$; thus $Z_{1x}$ is the atomic number if the heavy fragment is a complete ellipsoid with $(a_1,b_1)$ semiaxes. Variation of $Z_{1x}/A_{1x}$ must also comply to

$$\left(\frac{Z_{1x}}{A_{1x}}\right)_f=\frac{Z_0}{A_0}, \tag{3}$$

where $Z_0$ and $A_0$ are the final values corresponding to the compound nucleus and

$$\left(\frac{Z_{1x}}{A_{1x}}\right)_i=\frac{Z_1}{A_1}, \tag{4}$$

where $Z_1$ and $A_1$ are the initial values of the target nucleus. A variation law fulfilling these conditions is

$$\frac{Z_{1x}}{A_{1x}}=\frac{1}{A_0-A_1}\left[(A_{1x}-A_1)\frac{Z_0}{A_0}+(A_0-A_{1x})\frac{Z_1}{A_1}\right] \tag{5}$$

or

$$Z_{1x}(A_{1x})=\frac{A_{1x}}{A_0-A_1}\left[(A_{1x}-A_1)\frac{Z_0}{A_0}+(A_0-A_{1x})\frac{Z_1}{A_1}\right]. \tag{6}$$

For $A_{1x}=A_0$ we have $Z_{1x}=Z_0$ and for $A_{1x}=A_1$ results $Z_{1x}=Z_1$. We emphasize that $A_{1x}$, $Z_{1x}$, $A_{2x}$, and $Z_{2x}$ are not the real mass and atomic numbers, but the ones which correspond to whole non-intersected nuclei having the same semiaxes as the real intersected ones. The geometrical link to actual dimensions is made through Eq. (1). Similarly, for the light nucleus part of the overlapping configuration we have:

$$Z_{2x}(A_{2x})=\frac{A_{2x}}{A_0-A_2}\left[(A_{2x}-A_2)\frac{Z_0}{A_0}+(A_0-A_{2x})\frac{Z_2}{A_2}\right], \tag{7}$$

where $A_{2x}=a_2b_2^2/r_0^3$. Obviously, one should mention that $A_{1x}+A_{2x}\neq A_0$ and $Z_{1x}+Z_{2x}\neq Z_0$; in fact, $A_{1x}\geqslant A_{1i}$, $A_{2x}\geqslant A_{2i}$ and $Z_{1x}\geqslant Z_{1i}$, $Z_{2x}\geqslant Z_{2i}$, where $A_{1i}$, $Z_{1i}$ and $A_{2i}$, $Z_{2i}$ are the real intermediary masses and charges. As the overlapping region increases (the $R$ distance becomes smaller) both target and projectile shapes approach the final compound nucleus deformation $(b_0,a_0)$. In this way, at the final step we have

$$r_0^3A_{1x}=\pi a_1b_1^2\rightarrow\pi a_0b_0^2=r_0^3A_0,$$

$$r_0^3A_{2x}=\pi a_2b_2^2\rightarrow\pi a_0b_0^2=r_0^3A_0. \tag{8}$$

Then the two hypothetical atomic numbers $Z_{1x}$ and $Z_{2x}$ become

$$Z_{1x}(A_{1x}=A_0)=\frac{A_0}{A_0-A_1}(A_0-A_1)\frac{Z_0}{A_0}=Z_0,$$

$$Z_{2x}(A_{2x}=A_0)=\frac{A_0}{A_0-A_2}(A_0-A_2)\frac{Z_0}{A_0}=Z_0. \tag{9}$$

From these equations results, at the end of the fusion process,

$$\left(\frac{Z_{1x}}{A_{1x}}\right)_f=\left(\frac{Z_{2x}}{A_{2x}}\right)_f=\frac{Z_0}{A_0}. \tag{10}$$

The corresponding proton densities are

$$\rho_{p1}=\frac{Z_{1x}}{V_{1x}}=\frac{Z_{1x}}{\frac{4\pi}{3}a_1b_1^2},$$

$$\rho_{p2} = \frac{Z_{2x}}{V_{2x}} = \frac{Z_{2x}}{\frac{4\pi}{3} a_2 b_2^2}, \tag{11}$$

where $V_{1x}=(4\pi/3)a_1b_1^2$ and $V_{2x}=(4\pi/3)a_2b_2^2$ are the volumes of the ellipsoids corresponding to separate nuclei $(A_{1x},Z_{1x})$ and $(A_{2x},Z_{2x})$. But the real intermediary volumes are $V_1$ and $V_2$, with the same proton densities as $V_{1x}$ and $V_{2x}$, respectively. Hence the real intermediary atomic numbers $Z_{1i}$ and $Z_{2i}$ of the fusion shapes are

$$Z_{1i} = \frac{Z_{1x}}{V_{1x}} V_1 = \frac{Z_{1x}}{\frac{4\pi}{3} a_1 b_1^2} V_1 = \rho_{p1} V_1,$$

$$Z_{2i} = \frac{Z_{2x}}{V_{2x}} V_2 = \frac{Z_{2x}}{\frac{4\pi}{3} a_2 b_2^2} V_2 = \rho_{p2} V_2. \tag{12}$$

The squared charge densities are $\rho_{ei}^2=\rho_{pi}^2 1.44$. The analysis refers to adiabatic cold fusion process. Every step within the overlapping region towards the complete fusion is slow enough to allow nucleon rearrangement. Therefore the total volume is conserved. Since the number of nucleons remains the same, the total nucleon density is considered constant. With the simplifying hypothesis of constant mass density, we have for the intermediary mass numbers $A_{1i}$ and $A_{2i}$ and neutron numbers $N_{1i}$ and $N_{2i}$:

$$A_{1i} = \frac{V_1}{\frac{4\pi}{3} r_0^3}, N_{1i} = A_{1i} - Z_{1i}.$$

$$A_{2i} = \frac{V_2}{\frac{4\pi}{3} r_0^3}, N_{2i} = A_{2i} - Z_{2i}. \tag{13}$$

For the same fusion reaction, an ellipsoidal projectile can change its shape parameters $(a_2,b_2)$ in different ways along the overlapping region: it can preserve its initial $b_{20}$ semiaxis or $b_2$ can become larger up to the limit where $b_2=b_0$, the semiaxis of the compound nucleus. Between these two limits, $b_2$ can take any value, provided that the volume $V_2$ does not become larger then its initial value. Consequently, the corresponding intermediary atomic number $Z_{2i}$ changes according to the above considerations. In Fig. 2, upper part, the variation of $Z_{2x}$ with the normalized distance between centers $R_n=(R-R_f)/(R_t-R_f)$ is presented, where $R_f$ and $R_t$ are the final and the tangent configuration distances between centers. Different curves correspond to different laws of variation for the small semiaxis of $(A_{2i},Z_{2i})$. The plots refer to a superheavy nucleus synthesis: $^{54}\mathrm{Cr}+^{238}\mathrm{U}\rightarrow{}^{292}116$. The middle plot refers to the real intermediary atomic number variation $Z_{2i}$ with $R_n$. Variations in the last part of the fusion process $(R_n \leqslant 0.4)$ are due to volume differences. The smallest value for the $V_2$ volume is for $b_2=b_{20}(^{292}116)$ at the same $R_n$, the situation where the projectile preserves its initial semiaxes.

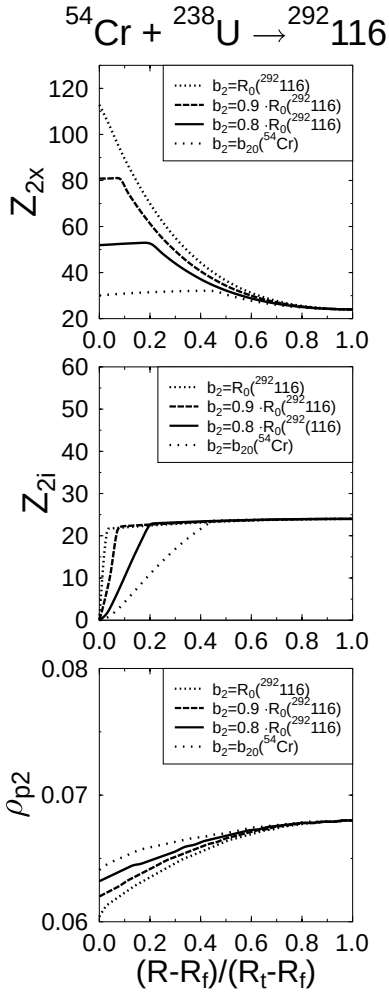


FIG. 2. Intermediary hypothetic atomic number $Z_{2x}$ (upper plot), real intermediary atomic number $Z_{2i}$ (middle plot), and charge density variation of the target nucleus in the synthesis of $^{292}116$.

The lower plot represents the proton density variation. The larger the volume, the lower the charge density, as can be seen. The highest proton density corresponds to $b_2=b_{20}(^{292}116)$, when the nonoverlapped part of the projectile remains almost at its initial shape.

### III. SINGLE-PARTICLE ENERGY LEVELS

The microscopic potential which follows the equipotentiality on the nuclear surface is generated by the ellipsoidally deformed two-center oscillators:

$$V^{(r)}(\rho,z) = \begin{cases} V_1(\rho,z) = \frac{1}{2}m_0\omega_{\rho_1}^2\rho^2 + \frac{1}{2}m_0\omega_{z_1}^2(z+z_1)^2, & v_1 \\ V_2(\rho,z) = \frac{1}{2}m_0\omega_{\rho_2}^2\rho^2 + \frac{1}{2}m_0\omega_{z_2}^2(z-z_2)^2, & v_2 \end{cases} \tag{14}$$

where $v_1$ and $v_2$ are the space regions where the two potentials are acting. These Hilbert space regions are defined by

$$V_1(\rho, z) = V_2(\rho, z). \tag{15}$$

The shape and the volume of $v_1$ and $v_2$ depend on the overlapping grade and $(A_1, Z_1)$ target and $(A_2, Z_2)$ projectile. Any change in the oscillator frequencies is converted to a change in $v_1$ and $v_2$. The four frequencies define the shape; when using the volume conservation $a_i b_i^2 = R_i^3$ and $\hbar\omega_i = 41 A_i^{-1/3}$, where $R_i = r_0 A_i^{1/3}$, one obtains the shape dependence of the frequencies

$$m_0\omega_{\rho_i}^2 = (a_i/b_i)^{2/3} m_0\omega_{0i}^2 = (a_i/b_i)^{2/3}\ 54.5/R_i^2,$$

$$m_0\omega_{zi}^2 = (b_i/a_i)^{4/3} m_0\omega_{0i}^2 = (b_i/a_i)^{4/3}\ 54.5/R_i^2 \tag{16}$$

with $i = 1, 2$. In this way the two-center oscillator potential for fusionlike shapes follows the changes of the two ellipsoidal partner deformations. The influence of the charge density on the potential manifests through Eqs. (11) and (16). In such a way the variation of the charge density is expressed by the variation of the four frequencies via the ellipsoid semiaxes.

Besides the overlapped deformed oscillator energies, charge density acts on the angular momentum dependent interactions. In order to assure hermicity of the matrices (due to the fact that strength parameters have specific values varying with the mass number), the anticommutator is used to obtain the spin orbit and the $\mathbf{l}^2$ term [12]:

$$V_{so} = \begin{cases} -\left\{ \dfrac{\hbar}{m_0\omega_{01}} \kappa_1(\rho, z), (\boldsymbol{\nabla} V^{(r)} \times \mathbf{p})\mathbf{s} \right\} & (v_1 \text{ region}) \\ -\left\{ \dfrac{\hbar}{m_0\omega_{02}} \kappa_2(\rho, z), (\boldsymbol{\nabla} V^{(r)} \times \mathbf{p})\mathbf{s} \right\} & (v_2 \text{ region}), \end{cases} \tag{17}$$

and similarly for the $V_{\mathbf{l}^2}$ term. It is important to observe that with the above form, the spin-orbit potential becomes shape dependent through the $\nabla V^{(r)}$ term.

The spin-orbit operator is calculated as usual using creation and annihilation components:

$$\Omega\mathbf{s} = \tfrac{1}{2}(\Omega^+\mathbf{s}^- + \Omega^-\mathbf{s}^+) + \Omega_z\mathbf{s}_z, \tag{18}$$

where

$$\Omega^+ = -e^{i\varphi}\left[ \frac{\partial V^{(r)}(\rho, z)}{\partial\rho}\frac{\partial}{\partial z} - \frac{\partial V^{(r)}(\rho, z)}{\partial z}\frac{\partial}{\partial\rho} - \frac{i}{\rho}\frac{\partial V^{(r)}(\rho, z)}{\partial z}\frac{\partial}{\partial\varphi}\right],$$

$$\Omega^- = e^{-i\varphi}\left[ \frac{\partial V^{(r)}(\rho, z)}{\partial\rho}\frac{\partial}{\partial z} - \frac{\partial V^{(r)}(\rho, z)}{\partial z}\frac{\partial}{\partial\rho} + \frac{i}{\rho}\frac{\partial V^{(r)}(\rho, z)}{\partial z}\frac{\partial}{\partial\varphi}\right],$$

$$\Omega_z = -\frac{i}{\rho}\frac{\partial V^{(r)}}{\partial\rho}\frac{\partial}{\partial\varphi}. \tag{19}$$

Strength parameters $\kappa_i(\rho, z)$ depend on the mass region and each of these regions corresponds to $v_1$ and $v_2$ space domains. For the same region $v_i$ we have a different $\kappa_i$ for protons and neutrons. As $v_1$, $v_2$ are determined by $V_1(\rho, z) = V_2(\rho, z)$, when frequencies (i.e. ellipsoid semiaxes) vary, so do the matrix elements of $\Omega\mathbf{s}$, in direct correspondence with charge density variation. The result is characterized by different proton and neutron level schemes for various charge density paths. Detailed matrix elements and level scheme calculation are described in Ref. [13]. The final energy levels of the synthesized system depend on the two perpendicular frequencies corresponding to the fused nucleus, $\omega_{\rho 0}$ and $\omega_{z0}$. At this point it is worth mentioning that, along the fusionlike shape sequences, the two crossing level schemes of the target and projectile *converge* toward the compound nucleus level scheme. This is possible only if the two partner frequencies $(\omega_{\rho 1}, \omega_{z1}; \omega_{\rho 2}, \omega_{z2})$ approach $(\omega_{\rho 0}, \omega_{z0})$. The final level energies will depend on $\omega_{\rho 0}, \omega_{z0}$ through the oscillator and spin-orbit potential:

$$V_0^{(r)}(\rho, z) = \tfrac{1}{2} m_0\omega_0^2\rho^2 + \tfrac{1}{2} m_0\omega_{z0}^2 z^2, \tag{20}$$

$$V_{so}^{(0)} = -\left\{ \frac{\hbar}{m_0\omega_0}\kappa_0(\rho, z), [\boldsymbol{\nabla} V_0^{(r)}(\omega_{\rho 0}, \omega_{z0}; \rho, z) \times \mathbf{p}]\mathbf{s} \right\} \tag{21}$$

and similarly for $V_{\mathbf{l}^2}$. Hence the frequency dependent potentials, as a consequence of Eqs. (20), (21), and (19), or with respect to the convergence of the energy levels, must follow a cycle like

$$V^{(r)} = V^{(r)}(\omega_{\rho 1}, \omega_{z1}; \omega_{\rho_2}, \omega_{z2}) \to V_0^{(r)}(\omega_{\rho 0}, \omega_{z0}),$$

$$V_{so} = V_{so}(\omega_{\rho 1}, \omega_{z1}; \omega_{\rho 2}, \omega_{z2}) \to V_{so}^{(0)}(\omega_{\rho 0}, \omega_{z0}) \tag{22}$$

and the same for $V_{\mathbf{l}^2}$. By taking into account the boundary conditions for $\omega_{\rho_i}, \omega_{zi}$ as a result of Eq. (22), two free parameters are likely to be modified: one is the semiaxis $b_2$ and the other is the ratio $\chi_2 = b_2/a_2$. Besides the boundary conditions, these parameters are subjected to nuclear volume conservation. Since $\chi_2$ and $b_2$ can take values over the range $(\chi_{20}, \chi_0)$, and $(b_{20}, b_0)$ respectively, two laws of variation fulfill the above conditions:

$$\chi_2(R, k) = \chi_0 + (\chi_{20} - \chi_0)\frac{R - R_f}{k\Delta R} \tag{23}$$

and

$$b_2(R, m) = b_0 - m\Delta b - [(b_0 - m\Delta b) - b_{20}]\frac{R - R_f}{R_t - R_f}, \tag{24}$$

where $\Delta R$ is the pace in $R$. At $R = R_f$ the projectile is completely embedded in the target. $k$ is the number of steps in $R$. In this work $\Delta R = 0.1$ fm. The maximum value of $k$, which is $k_{max}$, varies from $k_{max}^{(f)}\Delta R = R_f$ to $k_{max}^{(t)}\Delta R = R_t$. When $k_{max} = k_{max}^{(t)}$, $\chi_2$ starts to modify toward $\chi_0$ starting from the first step of overlapping, after the tangency. For $k_{max} = k_{max}^{(f)}$, the projectile preserves its initial semiaxis ratio all along the overlapping region; this is the situation when

the charge density of the nonoverlapped part of the projectile does not change during the fusion process. Finally, for $R=R_f$ we have $\chi_2=\chi_0$.

A similar analysis is available for the $b_1$ variation. The target deformation path is subjected to two similar equations for $\chi_1$ and $b_1$ as Eqs. (23) and (24). However, our calculations work only with $\chi_1$ as variable for the target, since $b_1$ is no more independent, due to total volume conservation. Consequently, another $\chi_1$ equation is functional with the same $k$ so that $b_1$ (thus $a_1$) is calculated from volume conservation. However, it is worth mentioning that a more complete analysis would comprise different $k$ values for target and projectile. Various maximal and minimal values for $k$ for the two partners produce a large possible range of deformation paths. A minimization procedure is compulsory to obtain the optimal pair of $k$'s for a given reaction. However, this work uses the same $k$ value for the target and projectile in order to emphasize the impact of this parameter on charge density variation.

Due to the volume conservation limitations [the nonoverlapped volume of $(A_2,Z_2)$ cannot exceed its initial value], the maximum value of $m$ is determined for every reaction channel. The final $b_2$ value is reached when $R=R_f$, whereas the initial one (touching point) stays for $R=R_t$:

$$b_2(R_t, m) = b_{20},$$

$$b_2(R_f, m) = b_{2f} = b_0 - m\Delta b, \tag{25}$$

where $\Delta b$ is the variation pace for the $b_2$ semiaxis. Equations (23) and (24) together with Eqs. (11) and (16) define the geometrical correspondence between charge density and nuclear shape changes.

Variations of $Z_{1x}/A_{1x}$ and $Z_{2x}/A_{2x}$ depend on $(a_1,b_1)$ and $(a_2,b_2)$, respectively, through Eq. (2) for the target and a similar equation for the projectile. Equations (6) and (7) are their laws of variation as functions of the intermediary hypothetical $A_{1x}$ and $A_{2x}$. But $A_{1x}$ and $A_{2x}$ are determined themselves by $a_1,b_1$ and $a_2,b_2$, respectively, through Eq. (8), i.e., $A_{1x}=A_{1x}(a_1,b_1)=A_{1x}(\chi_1,b_1)$ and $A_{2x}=A_{2x}(\chi_2,b_2)$. The independent quantities during the overlapping process are $\chi_1$, $\chi_2$ and $b_1$ and $b_2$; their variations are described by Eqs. (23) and (24) for the projectile and similarly to Eq. (23) for the $\chi_1$ target. The values of the parameters $k$ and $m$ in these equations are obtained by minimization of the total deformation energy. Any different value of $\chi_1$ or $\chi_2$ and $b_1$ and $b_2$ yields a different $A_{1x}$ and $A_{2x}$, or different $(\omega_{\rho_1},\omega_{z1})$ and $(\omega_{\rho_2},\omega_{z2})$ as well.

The level scheme sequence of the overlapping configurations through the fusion path is used as input for the calculation of the shell correction energy $E_{shell}$. Strutinsky method [14] is used separately for protons and neutrons, as corresponding to different nucleon numbers and different spin-orbit strength parameters $\kappa$, cf. Eq. (12). Mass number dependent $\kappa_p$ and $\kappa_n$ for protons and neutrons, respectively, act on $Z_{2i}$ and $N_{2i}$. As a result, $E_{shell}$ is calculated as charge density dependent.

## IV. MACROSCOPIC ENERGY

The macroscopic energy $E_{macro}$ is computed as the sum of the Coulomb $E_C$ [15] and the nuclear Yukawa-plus-expoenential term $E_Y$ [16]. The Coulomb term reads

$$E_C = \frac{2\pi}{3}\rho_e \int_{z_{min}}^{z_{max}} dz \int_{z_{min}}^{z_{max}} dz' F_C(z,z') \tag{26}$$

where

$$\begin{aligned} F_C(z,z') = \Bigg\{ & \rho(z)\rho(z')\frac{K(k)-2D(k)}{3} \times \Bigg[ 2[\rho^2(z)+\rho^2(z') \\ & -(z-z')^2] + 1.5(z-z')\left(\frac{d\rho^2(z')}{dz'} - \frac{d\rho^2(z)}{dz}\right)\Bigg] \\ & + K(k)\Bigg\{ \frac{\rho^2(z)\rho^2(z')}{3} \\ & + \left[\rho^2(z) - 0.5(z-z')\frac{d\rho^2(z)}{dz}\right] \\ & \times \left[\rho^2(z') + 0.5(z-z')\frac{d\rho^2(z')}{dz'}\right]\Bigg\}\Bigg\} \\ & \times \frac{1}{\{[\rho(z)+\rho(z')]^2 + (z-z')^2\}^{1/2}}, \end{aligned} \tag{27}$$

where

$$k^2 = \frac{4\rho(z)\rho(z')}{[\rho(z)+\rho(z')]^2 + (z-z')^2},$$

$$D(k) = \frac{K(k)-K'(k)}{k^2}, \tag{28}$$

and $\rho(z)$ is the surface equation. If $z=z'$ we have

$$F(z,z') = \frac{4\rho^3(z)}{3}. \tag{29}$$

For our two intersected nuclei system shape, the Coulomb energy can be written as [17]

$$E_C = \frac{2\pi}{3}(\rho_{e1}^2 F_{C1} + \rho_{e2}^2 F_{C2} + 2\rho_{e1}\rho_{e2}F_{C12}), \tag{30}$$

where

$$F_{C1} = \int_{-a_1}^{z_s} dz \int_{-a_1}^{z_s} dz' F_1(z,z'), \tag{31}$$

$$F_{C2} = \int_{z_s}^{R+a_2} dz \int_{z_s}^{R+a_2} dz' F_2(z,z'), \tag{32}$$

$$F_{C12} = \int_{-a_1}^{z_s} dz \int_{z_s}^{R+a_2} dz' F_{12}(z,z'). \tag{33}$$

The integrands read

$$F_i(z,z') = \left\{ \rho_i(z)\rho_i(z')\frac{K-2D}{3} + \left[ 2[\rho_i^2(z)+\rho_i^2(z') - (z-z')^2] + 1.5(z-z')\left(\frac{d\rho_1^2(z')}{dz'} - \frac{d\rho_i^2(z)}{dz}\right)\right] + K\left\{ \frac{\rho_i^2(z)\rho_i^2(z')}{3} + \left[\rho_i^2(z) - 0.5(z-z')\frac{d\rho_i^2(z)}{dz}\right] \times \left[\rho_i^2(z') + 0.5(z-z')\frac{d\rho_i^2(z')}{dz'}\right]\right\}\right\} \times \frac{1}{\{[\rho_i(z)+\rho_i(z')]^2 + (z-z')^2\}^{1/2}} \quad (34)$$

and $K=K(k)_i$, $K'=K'(k_i)$ with $i=1,2$, and

$$k_i^2 = \frac{4\rho_i(z)\rho_i(z')}{[\rho_i(z)+\rho_i(z')]^2 + (z-z')^2}. \quad (35)$$

The interaction term reads

$$F_{12}(z,z') = \left\{ \rho_1(z)\rho_2(z')\frac{K(k_{12})-2D(k_{12})}{3} \times \left[ 2[\rho_1^2(z)+\rho_2^2(z') - (z-z')^2] + 1.5(z-z') \times \left(\frac{d\rho_2^2(z')}{dz'} - \frac{d\rho_1^2(z)}{dz}\right)\right] + K(k_{12})\left\{ \frac{\rho_1^2(z)\rho_2^2(z')}{3} + \left[\rho_1^2(z) - 0.5(z-z')\frac{d\rho_1^2(z)}{dz}\right] \times \left[\rho_2^2(z') + 0.5(z-z')\frac{d\rho_2^2(z')}{dz'}\right]\right\}\right\} \times \frac{1}{\{[\rho_1(z)+\rho_2(z')]^2 + (z-z')^2\}^{1/2}} \quad (36)$$

with

$$k_{12}^2 = \frac{4\rho_1(z)\rho_2(z')}{[\rho_1(z)+\rho_2(z')]^2 + (z-z')^2}. \quad (37)$$

For the sphere the Coulomb energy is

$$E_{C0} = \frac{3Z^2e^2}{5r_0A^{1/3}}. \quad (38)$$

The Yukawa-plus-exponential energy $E_Y$ is [17]

$$E_Y = \frac{1}{4\pi r_0^2}[c_{s1}F_{EY1} + c_{s2}F_{EY2} + 2(c_{s1}c_{s2})^{1/2}F_{EY12}], \quad (39)$$

where [16]

$$F_{EY1} = \int_0^{2\pi}\int_{-a_1}^{z_s}\int_{-a_1}^{z_s} F_{Y1}^{(1)}F_{Y2}^{(1)}Q^{(1)}d\phi dz dz', \quad (40)$$

$$F_{EY2} = \int_0^{2\pi}\int_{z_s}^{R+a_2}\int_{z_s}^{R+a_2} F_{Y1}^{(2)}F_{Y2}^{(2)}Q^{(2)}d\phi dz dz', \quad (41)$$

$$F_{EY12} = \int_0^{2\pi}\int_{-a_1}^{z_s}\int_{z_s}^{R+a_2} F_{Y1}^{(12)}F_{Y2}^{(12)}Q^{(12)}d\phi dz dz'. \quad (42)$$

The terms in the integrand are

$$F_{Y1}^{(i)} = \rho_i^2(z) - \rho_i(z)\rho_i(z')\cos\phi - 0.5(z-z')\frac{d\rho_i^2(z)}{dz},$$

$$F_{Y2}^{(i)} = \rho_i^2(z') - \rho_i(z)\rho_i(z')\cos\phi + 0.5(z-z')\frac{d\rho_i^2(z')}{dz'},$$

$$Q^{(i)} = 2 - \left[\left(\frac{\sigma_i}{a}\right)^2 + 2\frac{\sigma_i}{a} - 2\right]e^{-\sigma_i/a}\frac{1}{\sigma_i^4},$$

$$\sigma_1 = [\rho_i^2(z) + \rho_i^2(z') - 2\rho_i(z)\rho_i(z')\cos\phi + (z-z')^2]^{1/2} \quad (43)$$

with $i=1,2$ and the interaction term

$$F_{Y1}^{(12)} = \rho_1^2(z) - \rho_1(z)\rho_2(z')\cos\phi - 0.5(z-z')\frac{d\rho_1^2(z)}{dz},$$

$$F_{Y2}^{(12)} = \rho_2^2(z') - \rho_1(z)\rho_2(z')\cos\phi + 0.5(z-z')\frac{d\rho_2^2(z')}{dz'},$$

$$Q^{(2)} = 2 - \left[\left(\frac{\sigma_{12}}{a}\right)^2 + 2\frac{\sigma_{12}}{a} - 2\right]e^{-\sigma_{12}/a}\frac{1}{\sigma_{12}^4},$$

$$\sigma_{12} = [\rho_1^2(z) + \rho_2^2(z') - 2\rho_1(z)\rho_2(z')\cos\phi + (z-z')^2]^{1/2}. \quad (44)$$

For the sphere

$$E_Y^{(0)} = \left\{ 1 - 3\left(\frac{a}{R_0}\right)^2 + \left(\frac{R_0}{a}+1\right) \times \left[2 + 3\frac{a}{R_0} + 3\left(\frac{a}{R_0}\right)^2\right]e^{-2R_0/a}\right\}E_S^{(0)}, \quad (45)$$

where

$$E_S^{(0)} = c_sA^{2/3}. \quad (46)$$

For the intermediate surface coefficients $c_{s1i}$ and $c_{s2i}$, with the general expression

$$c_{sji} = a_s(1-\kappa I_{ji}^2), \quad (47)$$

we use $A_{1i}, Z_{1i}$ from Eqs. (9) and (10), with $I_{ji}=(N_{ji}-Z_{ji})/A_{ji}$ where $j=1,2$.

The total macroscopic deformation energy is

$$E_{macro} = (E_C - E_C^{(0)}) + (E_Y - E_Y^{(0)}). \quad (48)$$

## V. RESULTS AND DISCUSSION

First results are presented for the light nuclei fusion reaction $^{36}Ar+^{66}Fe \rightarrow ^{102}Ru$. All the curves are drawn after mini-

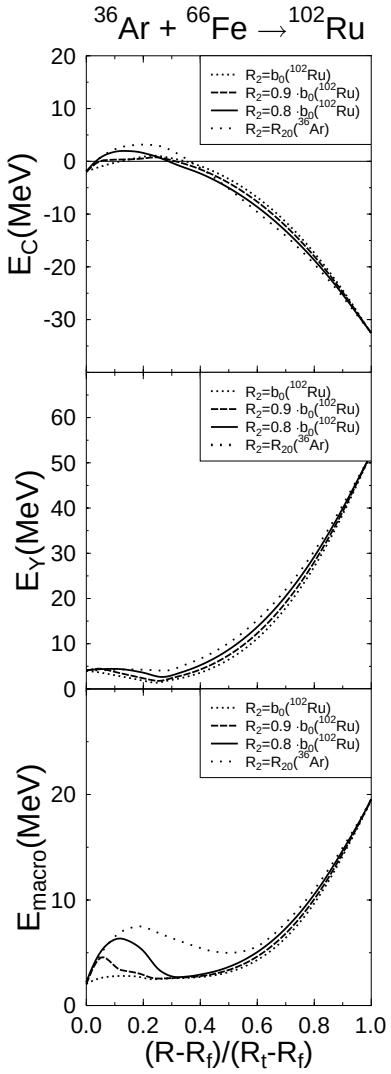


FIG. 3. Coulomb $E_C$ (upper plot), nuclear Yukawa-plus-exponential $E_Y$ (middle plot), and their sum $E_{macro}$ for four configuration paths corresponding to four different charge density variations for $^{102}$Ru synthesis.

mization against the $\chi$ parameter. The figures show only the variation as a function of $b_2$. $^{36}$Ar is spherical, with the initial radius $R_{20}(^{36}\mathrm{Ar})=3.3$ fm, $^{66}$Fe has an ellipsoidal deformation of $\beta_2^{(^{66}\mathrm{Fe})}=0.027$ and $^{102}$Ru is deformed with $\beta_2^{(^{102}\mathrm{Ru})}=0.189$. The projectile $^{36}$Ar maintains its spherical shape for the four possible paths presented in Figs. 3 and 4. This situation corresponds to $k=1$ in Eq. (23). For a different $k$, hence a different $\chi$ variation which implies ellipsoidal shape of the same projectile, the total deformation energy takes higher values. The macroscopic energies $E_C$ and $E_Y$ and their sum $E_{macro}$ have been computed with respect to the spherical shape values of $^{102}$Ru. Calculations have been performed for four values of the $m$ parameter [see Eq. (24)], defining four ways the charge density passes from projectile value to the compound nucleus one. During the overlapping process, the $^{36}$Ar radius becomes $R_2$ if the projectile preserves its spherical shape. The $R_2=b_0(^{102}\mathrm{Ru})$ curves correspond to the situation when the projectile ends the fusion process with its radius equal to the small semiaxis of $^{102}$Ru. The characteristics of these laws have been explained in Fig. 2. Figure 3 shows these four cases of shape sequences for macroscopic energies. Since for separated nuclei the energies do not differ, calculations are presented only for the overlapping region, i.e., for normalized distance $R_n=(R-R_f)/(R_t-R_f)<1$. Differences are more significant in the last part of the fusion process. Higher values of $E_C$ (upper plot), $E_Y$ (middle plot), and

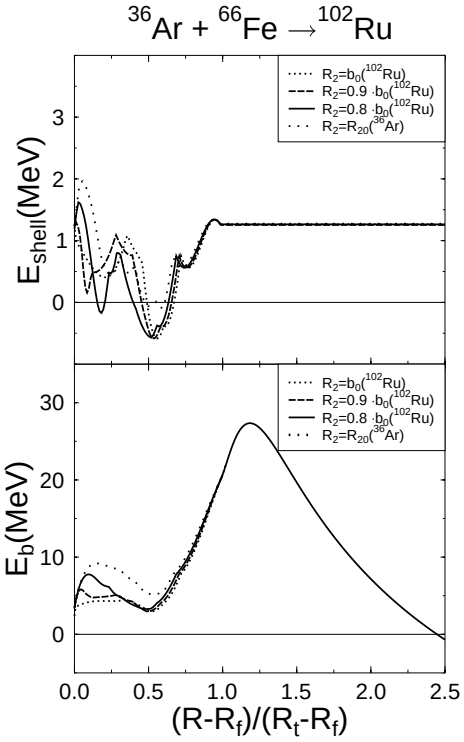


FIG. 4. Shell correction $E_{shell}$ (upper plot), and fusion barrier $E_b$ variation within the same four configuration paths as in Fig. 3, in $^{102}$Ru synthesis.

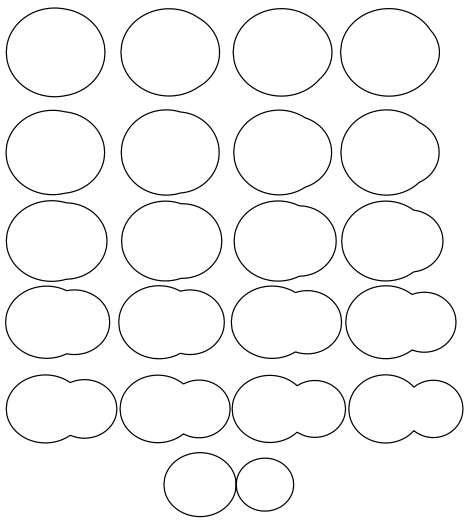

FIG. 5. The corresponding sequences of shapes for $^{102}$Ru; each column represents the path along each of the fusion barriers in Fig. 4.

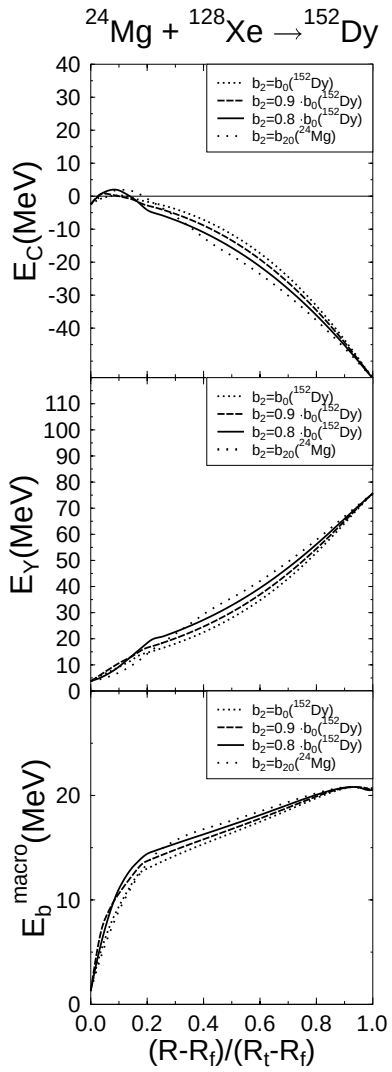


FIG. 6. Coulomb $E_C$ (upper plot), nuclear Yukawa-plus-exponential $E_Y$ (middle plot), and total macroscopic energy $E_{macro}$ for four configuration paths with projectile semiaxis ending at the values indicated in the box, for the synthesis of $^{152}$Dy.

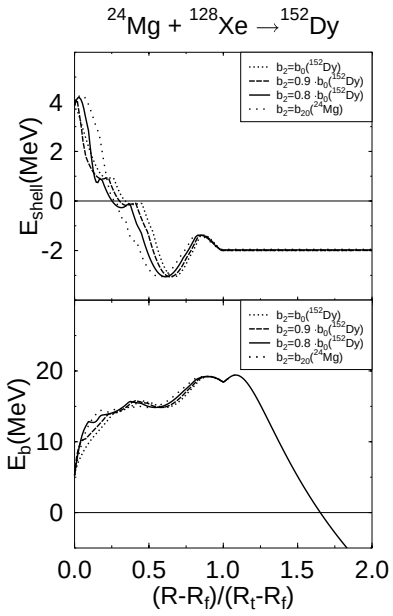


FIG. 7. Shell correction $E_{shell}$ (upper plot) and fusion barrier $E_b$ for the paths from Fig. 6, for the synthesis of $^{152}$Dy.

total macroscopic energy $E_{macro}$ correspond to the situation when $^{36}$Ar projectile preserves its initial radius $R_2 = R_{20}(^{36}\mathrm{Ar})$ until the end of the process. Intermediary situations are assigned by the two final $R_2$ values, 0.9 $b_0(^{102}\mathrm{Ru})$ and 0.8 $b_0(^{102}\mathrm{Ru})$. The lowest values are obtained when the projectile ends in the target with $R_2 = b_0(^{102}\mathrm{Ru})$. The bump in $E_{macro}$ at about $R_n = 0.2$ appears because of the higher charge density of the projectile shape, especially for $R_2 = R_{20}(^{36}\mathrm{Ar})$ (see Fig. 2). Maximum total macroscopic energy difference reaches 4 MeV between largest and smallest projectile radius curves, or between lowest and highest charge density values at the same $R_n$. Microscopic influence is depicted in Fig. 4 for $^{102}$Ru synthesis and the same four charge density variation paths. $R_n$ takes values far beyond the touching distance ($R_n > 1$), in order to comprise the whole cold fusion barrier. The variation of $E_{shell}$ (upper plot) nears 2 MeV and is more pronounced in the last part of the fusion process, as $(R - R_f)/(R_t - R_f)$ approaches zero. There is a mixed behavior of the four curves. The lowest values are successively reached by $R_2 = b_0(^{102}\mathrm{Ru})$ at the beginning of the process, then by $R_2 = 0.8\ b_0(^{102}\mathrm{Ru})$ followed by $0.9\ b_0(^{102}\mathrm{Ru})$ curve in the last part. The total sum $E_b = E_{macro} + E_{shell}$ is shown in the lower plot of Fig. 4. Differences of about 4 MeV are visible when $R_n$ approaches zero, and the situations when the projectile enlarge its dimensions as to seize synthesized nucleus size and shape are favored [$R_2 = b_0(^{102}\mathrm{Ru})$]. A remarkable feature is the appearance of minimum at $(R - R_f)/(R_t - R_f) = 0.5$. Such a shape isomerism has already been presumed in light nuclei fusion reactions [18,19], but it is only within this work that a minimum is obtained along the deformation energy for a certain reaction channel, for a dinuclear system. A comprehensive geometric correspondence of the different cold fusion paths can be observed in Fig. 5. The starting point of the fusion process is the touching configuration, depicted in the lowest part of the figure. Every column is the shape sequence matching to one of the barriers from Fig. 4. First column shows the situation when the projectile ends its total overlapping with $R_2 = b_0(^{102}\mathrm{Ru})$. The next two columns are drawn for $R_2 = 0.9\ b_0(^{102}\mathrm{Ru})$ and $0.8\ b_0(^{102}\mathrm{Ru})$, respectively, and the last one is the sequence for $R_2 = R_{20}(^{36}\mathrm{Ar})$.

The next cold fusion reaction which has been analyzed is $^{24}\mathrm{Mg} + ^{128}\mathrm{Xe} \rightarrow ^{152}\mathrm{Dy}$. All three partners are ellipsoidally deformed ($\beta_2^{(^{128}\mathrm{Xe})} = 0.143$, $\beta_2^{(^{24}\mathrm{Mg})} = 0.374$, and $\beta_2^{(^{152}\mathrm{Dy})} = 0.153$). In Fig. 6 macroscopic energy behavior is depicted, with the Coulomb term $E_C$ in the upper plot, nuclear Yukawa-plus-exponential term $E_Y$ in the middle plot and their sum $E_{macro}$ in the lower plot. Calculations have been performed for the same four charge density variation paths, i.e., the same variations for the projectile small semiaxis $b_2$. Though the shapes of the macroscopic barriers are different, their behaviors have the same characteristics. Differences are lower than in the previous case. A bump in $E_C$ slightly visible for $b_2 = b_{20}(^{24}\mathrm{Mg})$ disappears completely for $b_2 = b_0(^{152}\mathrm{Dy})$. The lowest values of $E_{macro}$ correspond again to the situation

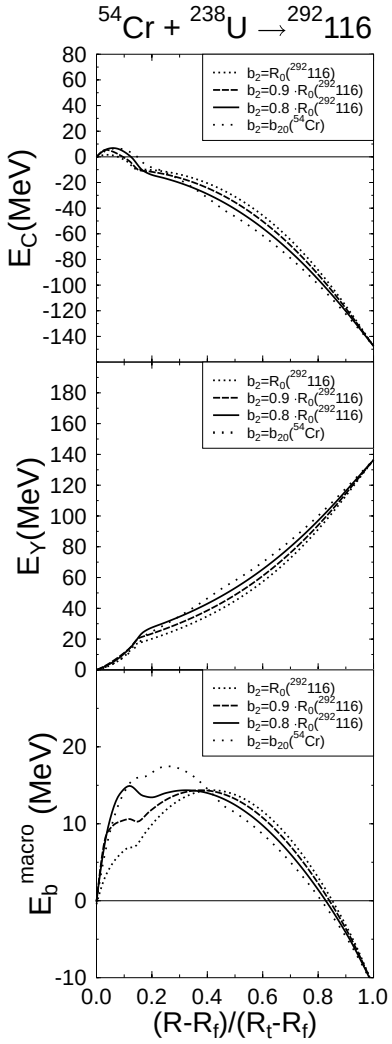


FIG. 8. Coulomb $E_C$ (upper plot), nuclear Yukawa-plus-exponential $E_Y$ (middle plot), and macroscopic $E_{macro}$ for four different transition configuration paths (the final values of $b_2$ are indicated in boxes), in the synthesis of the superheavy nucleus $^{292}116$.

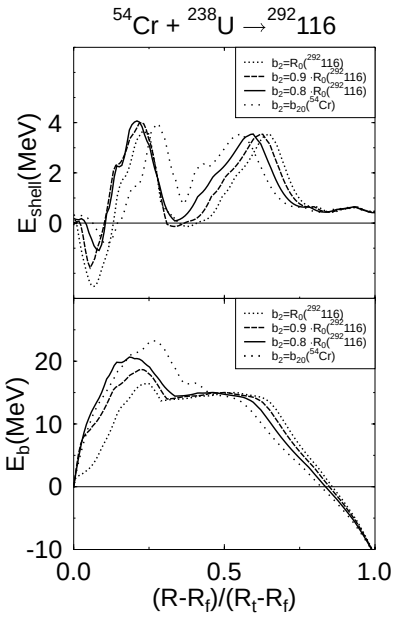


FIG. 9. Shell correction $E_{shell}$ (upper plot) and fusion barrier $E_b$ for the four paths indicated in Fig. 8, in the synthesis of $^{292}116$.

where the $^{24}$Mg projectile enlarge its dimensions so as to reach the synthesized $^{152}$Dy proportions [$b_2=b_0(^{152}\mathrm{Dy})$ curves]. This configuration path assures the smoothest pass of the charge density from projectile to compound nucleus value, but still only macroscopic terms are involved here. Shell corrections for the same reaction are depicted in Fig. 7, upper plot. Their values stretch from −3 MeV to 4.2 MeV. The lowest $E_{shell}$ values are first reached for $b_2=b_0(^{152}\mathrm{Dy})$ curve, but then for $b_2=b_{20}(^{24}\mathrm{Mg})$ followed by $b_2=0.8\ b_0(^{152}\mathrm{Dy})$ values are lower. Significant differences in the total deformation energy $E_b$ (lower plot) appear toward the end of the fusion process. Again $b_2=b_0(^{152}\mathrm{Dy})$ curve has the smallest energy values. The gain in lowering the total deformation energy by minimization against $\chi_2$ and $b_2$ is up to 3.7 MeV.

Finally a superheavy synthesis reaction is analyzed, $^{54}\mathrm{Cr}+^{238}\mathrm{U}\rightarrow{}^{292}116$. Both target and projectile are deformed with $\beta_2^{(^{54}\mathrm{Cr})}=0.180$ and $\beta_2^{(^{238}\mathrm{U})}=0.215$. The superheavy $^{292}116$ is considered spherical, with radius $R_0(^{292}116)=6.63$ fm. Macroscopic components are displayed in Fig. 8 for the same four $b_2$ variation laws. Despite the larger differences around $R_n=0.7$ in $E_C$ (upper plot) and $E_Y$ (middle plot), the significant variations in the total macroscopic energy $E_{macro}$ appear at the end of the process, for $(R-R_f)/(R_t-R_f)<0.4$. This is due to the fact that lower $E_C$ corresponds to higher $E_Y$ for the same $b_2$ law of variation, like it is easily visible for $b_2=R_0(^{292}116)$ curve. The lowest values for $E_{macro}$ are obtained for $b_2=R_0(^{292}116)$ curve at the end of fusion. Shell effects do not change the order. The $b_2=R_0(^{292}116)$ curve for $E_{shell}$ (Fig. 9, upper plot) has not always the lowest values: at the beginning of the overlapping region it is the $b_2=b_{20}(^{54}\mathrm{Cr})$ path which produces lower shell corrections. Then all four variation curves mix. At the end, again $b_2=R_0(^{292}116)$ is favored. This trend is transmitted to the total deformation energy $E_b$ (Fig. 9, lower plot). Close to the tangent point the $b_2=b_{20}(^{54}\mathrm{Cr})$ curve displays lower $E_b$ values. It is the situation where $^{54}$Cr keeps its semiaxis ratio *and* $b_2$ at its initial values. This part corresponds to the highest charge density, the initial charge density value of the projectile (see Fig. 2). Around $(R-R_f)/(R_t-R_f)=0.4$ the small semiaxis tends to increase toward $R_0(^{292}116)$. This volume enhancement induces the charge density decrease down to the synthesized superheavy $\rho_e$ value. Differences between curves reach 8 MeV, a rather large value for the cold fusion total deformation energy variation.

All the above results demonstrate the necessity of taking into account the charge density as a free parameter. Its influence is directly related to geometrical characteristics of the fusionlike shape, as the semiaxis ratio $\chi$ and the small semiaxis $b_2$ quantities. Minimization against these two parameters produces a significant decrease in barrier height.

## VI. CONCLUSION

Charge density influence on cold fusion barriers manifests itself through geometrical parameters characterizing the tar-

get and projectile nuclei within the overlapping region. Changes of semiaxis ratios and magnitude trigger a modification in proton density over the nonoverlapped volume of the projectile. As a free coordinate, charge density can lower the cold fusion deformation energy, as a result of minimization against $b_2$ and $\chi_2$. This kind of influence is especially active in the last part of the fusion process, when the projectile is already half embedded in the target ($R_n<0.5$) up to total synthesis. For light and intermediate nuclei cold fusion, the energy variation in the last part of the deformation path reaches 4 MeV for $^{102}$Ru and 3.7 MeV for $^{152}$Dy synthesis. For a possible superheavy production channel, influence of charge density changes is quantitatively more important. Energy differences in the cold fusion channel barrier of $^{292}$116 reach about 8 MeV in the last part of the overlapping process as a result of energy minimization. These very large energy deviations appear both in macroscopic and shell correction curves. Due to the exponential dependence of the penetrability factor on the deformation energy (via the action integral) such a variation is expected to be quantitatively significant. As a general trend, projectile tends to increase the volume of its nonoverlapped part toward the final stage of the fusion, approaching the synthesized nucleus geometry. Finally this work emphasizes the importance of calculating the *whole* fusion barrier shape. It is not only the height (which usually occurs at the very beginning of the process for light nuclei and in the middle of partially overlapping configuration for superheavy synthesis), but also the last part of the barrier which influences the process. We mention that the tip to tip collision is only the energetically favorized situation, corresponding to target-projectile axes angle $\theta=0$. A complete procedure implies separate analysis for rotation angles $\theta>0$. Such a complete calculation could enhance the value of the total cross section. Due to different target orientations, charge density follows other paths than those obtained by minimization of deformation energy at $\theta=0$.

## ACKNOWLEDGMENTS

This work was partly supported by UNESCO (UVEROSTE Contract No. 875.737.2); the Centre of Excellence IDRANAP under Contract No. ICA1-CT-2000-70023 with European Comission, Brussels; Bundesministerium fuer Bildung und Forschung (BMBF), Bonn, Gesellschaft fuer Schwerionenforschung, Darmstadt and Ministry of Education and Research, Bucharest.

[1] C. Y. Wong, Phys. Rev. Lett. **31**, 766 (1973).
[2] L. C. Vaz and J. M. Alexander, Phys. Rev. C **18**, 2152 (1978).
[3] B-A. Li and S. J. Yennelo, Phys. Rev. C **52**, R1746 (1995).
[4] K. Satou, H. Ikezoe, S. Mitsuoka, K. Nishio, and S. C. Jeong, Phys. Rev. C **65**, 054602 (2002).
[5] R. K. Gupta and D. R. Saroha, Phys. Rev. C **30**, 395 (1984).
[6] M. Colonna, M. DiTorro, G. Fabri, and S. Maccarone, Phys. Rev. C **57**, 1410 (1998).
[7] T. Rumin, K. Hagino, and N. Takigawa, Phys. Rev. C **63**, 044603 (2001).
[8] K. Nishio, H. Ikezoe, S. Mitsuoka, and J. Lu, Phys. Rev. C **62**, 014602 (2000).
[9] L. C. Vaz and J. M. Alexander, Phys. Rev. C **10**, 464 (1974).
[10] A. S. Jensen and C. Y. Wong, Phys. Rev. C **1**, 1321 (1970).
[11] W. Scobel, A. Mignerey, M. Blann, and H. H. Gutbrod, Phys. Rev. C **11**, 1701 (1975).
[12] J. Maruhn and W. Greiner, Z. Phys. A **251**, 431 (1972).
[13] R. A. Gherghescu, Phys. Rev. C **67**, 014309 (2003).
[14] V. Strutinsky, Nucl. Phys. **A95**, 420 (1967).
[15] K. T. Davies and A. J. Sierk, J. Comput. Phys. **18**, 311 (1975).
[16] H. J. Krappe, J. R. Nix, and A . J. Sierk, Phys. Rev. C **20**, 992 (1979).
[17] D. N. Poenaru, M. Ivascu, and D. Mazilu, Comput. Phys. Commun. **19**, 205 (1980).
[18] C. Beck *et al.*, Phys. Rev. C **63**, 014607 (2001).
[19] E. Gadioli *et al.*, Heavy Ion Phys. **7**, 275 (1998).